Reverberation Mapping Analysis of the 2016 HST Campaign on NGC 4593

Lukas Diehl

George-August-Universität Göttingen

January 18, 2026

Abstract

Abstract

Contents

List of Figures

List of Tables

1. Introduction

Active galactic nuclei (AGNs) are among the most luminous objects in the universe, emitting radiation across the entire electromagnetic spectrum (Netzer 2013). Unlike inactive galaxies such as the Milky Way, the supermassive black hole (SMBH) in an active galaxy continues to accrete matter from its central region. This process generates thermal radiation (Peterson 1997) as well as non-thermal emission such as photoionization and subsequent recombination (Netzer 2013). AGN show strong variability across the entire electromagnetic spectrum, with timescales ranging from hours to days (Ulrich et al. 1997).

A particularly interesting example is the barred spiral galaxy NGC 4593. NGC 4593 shows strong variability from the X-ray to the optical bands (McHardy et al. 2017; Cackett et al. 2018) with several strong broad emission lines, including Balmer lines, Lyman lines and helium lines, among others (Kollatschny & Dietrich 1997; Cackett et al. 2018; Ochmann et al. 2025). Several studies have analysed the structure and kinematics of NGC 4593 (e.g. (Kollatschny & Dietrich 1997; Denney et al. 2006; Cackett et al. 2018)) using reverberation mapping (RM) of the broad emission lines. This method uses measurable time lags between the response of the emitting regions to variations in the ionizing continuum to probe the structure and size of the broad-line region (Peterson 1993).

In a recent work, Cackett et al. 2018 conducted an observation campaign using the Hubble Space Telescope (HST) with the Space Telescope Imaging Spectrograph (STIS), between 12 July and 6 August 2016 on NGC 4593, covering wavelength ranges from about 1100 Å to 1700 Å and from 3900 Å to 9000 Å. This work focused on the reverberation of the accretion disk of NGC 4593 by analyzing the UV and optical continua (Cackett et al. 2018). This dataset allows me to perform a classical reverberation mapping analysis of the broad emission-lines based on these data, and to determine the mass of the SMBH.

Furthermore, NGC 4593 shows strong emission in the $OI\,\lambda8446$ emission line and the $Ca\,II\,\lambda8498\,\lambda8542\,\lambda8662$ triplet (Ochmann et al. 2025). These low-ionization lines have not yet been included in RM campaigns yet. The $OI\,\lambda8446$ emission line is

particularly interesting, as it can get enhanced through Bowen fluorescence (Bowen 1947; Grandi 1980). Its presence allows the variability and time lag to be measured from a HST/STIS RM campaign for the first time.

2. Scientific Background

2.1 Active Galactic Nuclei

Active Galactic Nuclei (AGNs) refer to the central region of active galaxies. These objects are among the most luminous in the universe, with bolometric luminosities ranging from 10^{41} to 10^{48} erg s^{-1}, outshining entire galaxies by several orders of magnitude (Peterson 1997). Historically, several stellar-based models were proposed, such as dense star clusters or supermassive stars. However, these scenarios were discarded, as they are expected to collapse into black holes themselves, and they cannot provide the required energy output. Today, it is understood that the enormous luminosities of AGN are powered by accretion of matter onto a supermassive black hole (SMBH) at the centers of galaxies (Rees 1984). The most widely accepted model for this accretion is a hot, rotating accretion disk surrounding the SMBH, which produces most of the observed radiation (Shakura & Sunyaev 1973). The following sections will outline the key components of an AGN and its variability, which is central to reverberation mapping analysis.
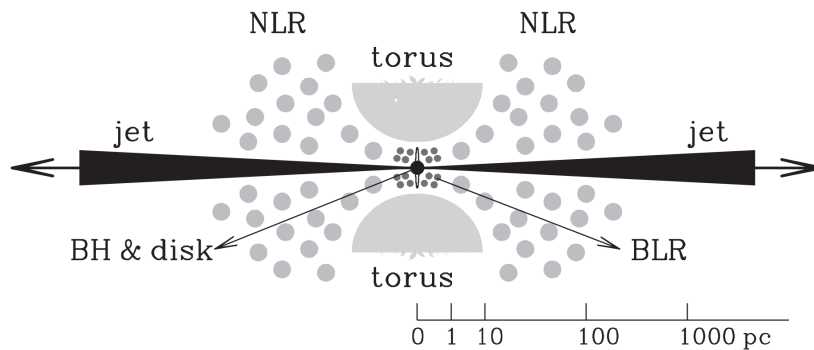
Figure 2.1: Different components of an AGN. Adopted from (Mo et al. 2010) Figure 14.3.

2.1.1 Structure and Spectral Features of an AGN

Figure 2.1 shows a schematic illustration of an AGN, consisting of a central super-massive black hole (SMBH), a surrounding accretion disk, a dusty torus and ionized gas regions known as the broad-line region (BLR) and narrow-line region (NLR). In some cases, relativistic jets are launched perpendicular to the plane of the accretion disk (Urry & Padovani 1995). The following subsections describe the physical components of AGN and the spectral features associated with them.

Supermassive Black Hole and Accretion Disk

The center of an AGN is defined by a supermassive black hole (SMBH), with typical masses between $10^6 \, M_\odot$ and $10^9 \, M_\odot$ (Peterson et al. 2004). It does not contribute to the AGN spectrum directly, but acts as the central engine driving observed spectral features of the AGN. It dominates the gravitational potential and, unlike inactive galaxies such as the Milky Way, it is surrounded by an accretion disk. Through viscous processes within the disk, such as turbulent friction and magneto-rotational instability, the angular momentum of the matter is transported outward, which leads to a spiraling inflow of matter toward the SMBH (Shakura & Sunyaev 1973). Several models have been proposed to describe the accretion process. The most widely used model is the geometrically thin and optically thick accretion disk, which consists of ionized gas in differential rotation around the SMBH (Shakura & Sunyaev 1973; Netzer 2013). The disk is composed primarily of ionized hydrogen and helium, with trace amounts of heavier elements (Netzer 2013). It extends from the innermost stable circular orbit (ISCO) near the event horizon out to distances of several light-days. The radial extent of the disk is relatively small compared to galactic scales and typically ranges from a few light-hours to a few light-days, corresponding to about 10^{-3} to $10^{-2} \, \mathrm{pc}$ (Shakura & Sunyaev 1973; Netzer 2013).

During the accretion process a substantial fraction of the gravitational energy of the matter is transformed into thermal radiation, which accounts for the enormous luminosity observed in AGNs and heats the accretion disk to high temperatures that depend on the mass of the SMBH (Netzer 2013). For example, the maximum effective temperature for an accretion disk around a SMBH with $M = 10^8, M_\odot$ is on the order of several $\times 10^5$ K, leading to UV and optical emission (Shakura & Sunyaev 1973; Netzer 2013). By contrast, disks around stellar-mass black holes reach much higher temperatures (up to a few $\times 10^6$ K), and therefore emit mostly in X-rays (Shakura & Sunyaev 1973; Netzer 2013). Due to the radial temperature gradient, the emitted spectrum cannot be described as a single blackbody. Instead, it results

from a superposition of many blackbody-like components at different temperatures, often referred to as a multicolour black-body (Netzer 2013). This produces a broad optical–UV continuum of ionizing photons, which interact with gas clouds near the nucleus and play a crucial role in shaping the spectral features of the BLR and NLR. These photons cause photoionization followed by recombination, which gives rise to the strong emission lines that are characteristic of AGN spectra (Netzer 2013).

Broad-Line and Narrow-Line Region

The ionized gas clouds near the nucleus can be divided into the broad-line region (BLR) and the narrow-line region (NLR). Both regions differ in density, distance from the SMBH, and the observed line widths (Urry & Padovani 1995). The BLR is located close to the nucleus, at distances ranging from a few light-days to a few light-years from the central SMBH (Goad et al. 2012)(see Figure 2.1). It consists of dense gas clouds with electron densities of $n_e \approx 10^{11}\,\mathrm{cm}^{-3}$, moving at velocities of several thousand $\mathrm{km\,s}^{-1}$ due to the strong gravitational influence of the SMBH. These velocities lead to significant Doppler broadening of permitted emission lines, with widths of $(500\text{–}10{,}000)\,\mathrm{km\,s}^{-1}$ (Peterson 1997). As described earlier, the BLR is photoionized by the continuum radiation emitted from the accretion disk. Consequently, the line emission from this region responds to changes in the continuum, leading to a strong correlation between the two and strong variability (Netzer 2013). This relationship is particularly relevant for reverberation mapping, which will be discussed later in Section 2.2.

Modelling the geometry of the BLR is challenging, because several emission lines have to be considered, whose intensities vary in response to changes in the continuum radiation (Netzer 2013). A common model assumes a spherical distribution of clouds connected to the accretion disk and located between the accretion disk and the dusty torus (Goad et al. 2012). Broad emission lines arise from permitted transitions such as Hα, Hβ, and Lyα (Netzer 2013).

The narrow-line region (NLR) extends out to several hundred parsecs from the central region (Peterson 1997). The gas in this region moves at much lower velocities, resulting in emission lines with widths typically of order $(350\text{–}400)\,\mathrm{km\,s}^{-1}$ (Peterson 1997). In contrast to the BLR, the NLR exhibits both permitted and forbidden transitions. Forbidden lines, such as [O III] $\lambda5007$, are prominent in the NLR because at its low densities ($n_e \sim 10^2\text{–}10^4\,\mathrm{cm}^{-3}$) collisional de-excitation is rare, allowing radiative decay from metastable levels (Peterson 1997). Due to its much larger extent compared to the BLR, the NLR responds only very slowly to

variations in the ionizing continuum. Therefore, the flux of the narrow emission lines can be treated as constant over timescales of several years (Peterson 1993). Because permitted emission lines can also originate in the NLR, multi-component emission-line profiles can be observed in AGN spectra (Peterson 1997).

Dusty Torus

Surrounding the accretion disk and the broad-line region is the dusty torus, a geometrically thick, optically dense structure composed of gas and dust. It extends from the radius at which dust can survive the intense radiation from the accretion disk out to scales of a few parsecs (Netzer 2013). The torus likely has a clumpy distribution and plays a crucial role in the unified model of AGNs (Urry & Padovani 1995; Netzer 2013). The dust in the torus absorbs a significant fraction of the UV and optical radiation emitted by the accretion disk and re-emits it thermally in the infrared. As a result, AGNs typically exhibit strong infrared emission, with the peak wavelength depending on the dust temperature in the torus (Netzer 2013). Even when the central region is hidden from direct view by the torus, this reprocessed infrared emission remains observable. It therefore provides a characteristic signature of obscured AGN activity and enables indirect constraints on the otherwise hidden central engine (Netzer 2013).
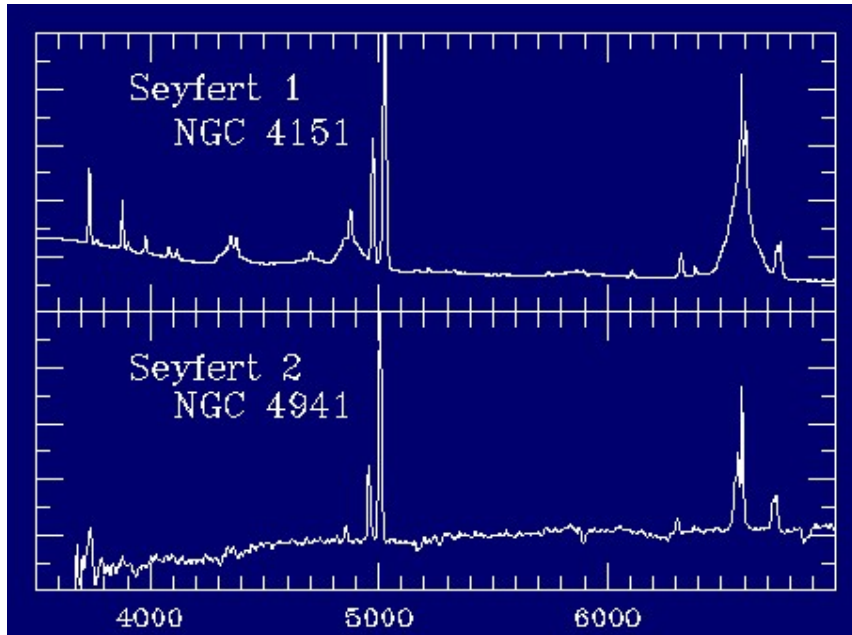

Figure 2.2: An example of Seyfert I and Seyfert II spectra illustrating their differences. Broad lines, such as the highlighted $H\alpha$ and $H\beta$, are only present in the Seyfert I spectrum, whereas forbidden [O III] lines are visible in both cases. Adapted from (Keel 2002).

2.1.2   Classification

AGNs get classified in subgroups based on their spectral features, which are strongly dependent to their intrinsic structure. The key parameters for this classification are luminosity, emission-line profiles and radio properties. Based on those parameters AGN get grouped into Seyfert galaxies, quasars and radio galaxies. They get further subdivided based on the appearance of broad and narrow emission lines. Some examples for these sub-classes are narrow-line Seyfert I galaxies (NLS1s), low-ionization nuclear emission-line regions (LINERs), and jet-dominated sources such as BL Lac objects or blazars (Antonucci 1993; Urry & Padovani 1995).

Seyfert Galaxies

Seyfert galaxies are named after Carl K. Seyfert, who in 1943 observed spiral galaxies characterized by exceptionally bright nuclei and strong emission lines in their optical spectra (Seyfert 1943). They are mainly classified into the sub-classes Seyfert I and Seyfert II based on the presence of broad emission lines. Figure 2.2 highlights the differences of the spectra of Type I and Type II Seyfert galaxies.

Seyfert I galaxies, such as NGC 4593, show both broad and narrow emission lines in their optical spectra. The broad lines, such as $H\alpha$ and $H\beta$, typically have full widths at half maximum (FWHM) of several thousand kilometers per second and from the fast-moving, high-density gas in the BLR (Peterson 1997). In contrast, narrow lines, including prominent forbidden transitions like [O III] $\lambda5007$ or [N II] $\lambda6584$, originate from the slow-moving, low-density gas in the NLR (Peterson 1997). The presence of both components in the spectrum allows for a clear classification as a Seyfert I galaxy, which is the case for NGC 4593. Further details on NGC 4593 are provided in Section 3.1. Between the two main Seyfert classes, several intermediate subclasses (1.2, 1.5, 1.8, 1.9) are defined based on the ratio of the broad towards the narrow components in the optical spectrum (Osterbrock 1977; Osterbrock 1981; Peterson 1997). Seyfert 1.8 and 1.9 galaxies show very weak broad components. In Seyfert 1.9 objects, the broad component is visible only in the Hα line, whereas in Seyfert 1.8 objects it is also detectable in Hβ. Furthermore, if the broad and narrow components in Hβ are of equal strength, the AGN is classified as a Seyfert 1.5 (Peterson 1997). If the narrow component is even weaker than the broad component, it is classified as a Seyfert 1.2 (Osterbrock 1977). The fact that the optical spectrum shows multi-component lines with both broad and narrow components, suggests that these emission lines originate in the BLR and the NLR in the respective ratio (Peterson 1997).

In comparison, Seyfert II galaxies completely lack these broad components in their optical spectra, likely due to orientation-dependent obscuration by the dusty torus. Following that the classification of a Seyfert galaxies strongly depends on the viewing angle of the observer, which is the key point for the Unified Model of AGN, which will deepened in section 2.1.3 (Peterson 1997).

Another notable subclass is the group of so-called narrow-line Seyfert I galaxies (NLS1s). They show most of the features of Seyfert 1 or 1.5 galaxies, except that the usually broad lines, such as the H I or He I lines, exhibit FWHM values that are only slightly larger than those of the narrow lines. They show a wide dispersion of spectral properties, with some objects have very strong Fe II emission, whereas others show almost none. This indicates that NLS1s do not form a homogeneous class (Osterbrock & Pogge 1985). NLSls are thought to have low-mass black holes accreting at high Eddington rates, suggesting they may represent a young evolutionary phase of AGN activity(Peterson 2011; Netzer 2013). Another possible explanation is an orientation effect. Another possible explanation is an orientation effect. When an NLS1 is observed at a very low inclination, the projected velocities are reduced, which leads to smaller observed Doppler broadening and therefore to narrow lines (Osterbrock & Pogge 1985).

Additional AGN Classes

In addition to Seyfert galaxies, there are several other classes of AGN. Quasars, which stands for quasi-stellar radio sources, are even more luminous than Seyfert galaxies and are typically found at higher redshifts. While the host galaxies of Seyfert galaxies are still observable, quasars completely outshine their host galaxies. Since quasars show similar emission characteristics to Seyfert galaxies, the modern distinction is based mainly on luminosity: quasars are classified as high-luminosity AGNs, while Seyfert galaxies represent the lower-luminosity end (Netzer 2013).

Radio galaxies form another important AGN class, distinguished by their strong radio emission and prominent jets, typically found in elliptical host galaxies. When their jets are aligned close to our line of sight, they are observed as blazars or BL Lac objects, which exhibit rapid variability and featureless optical spectra due to relativistic beaming (Netzer 2013).

Finally, LINERs are low-luminosity AGNs with spectra dominated by low-ionization emission lines. The physical origin of their ionization mechanism is still debated, and in some cases, they may not be powered by accretion at all (Netzer 2013).

While these classifications are based primarily on spectral characteristics, many

of the observed differences between AGN types can be attributed to orientation effects. The Unified Model of AGN provides a framework that explains this apparent diversity through a common internal structure, viewed from different angles.

2.1.3 Unification Model

Figure 2.3 shows an illustration of the Unification Model, which was postulated by Robert Antonucci in 1993. He proposed that the visible differences in AGN spectra are not due to fundamentally different structures. Instead, they arise mainly from the viewing angle toward the AGN center and from obscuration by the dusty torus (Antonucci 1993).

The figure shows with what type the same AGN would get classified depending on the observers viewing angle. Like mentioned before, the dusty torus plays a key role here, as it surrounds the central region of the AGN, the accretion disk and the fast-moving BLR. If the observer's line of sight is blocked by the torus, only radio emission, the optical/UV continuum and narrow-line emission from the NLR outside the torus can be detected. In this case, the AGN is classified as a Seyfert 2 galaxy, as the broad emission lines originating from the BLR are obscured and the optical/UV continuum from the accretion disk is only partially visible. The observer essentially views the AGN from a flat angle, looking directly at the torus.If, on the other hand, the observer has a direct view into the central region of the AGN, not obscured by the torus, the fast moving gas clouds of the BLR as well as the optical/UV emission continuum from the accretion disk become visible. In this case, both broad and narrow emission lines are visible, meaning the AGN is classified as a Seyfert 1 galaxy. (Urry & Padovani 1995).

The same principle applies to other AGN classes. Quasars can be considered the high-luminosity counterparts of Seyfert galaxies, where orientation and torus obscuration likewise affect their observed properties. Blazars, on the other hand, are seen when the relativistic jet is aligned closely with the observer's line of sight, leading to strong Doppler boosting, which makes the radiation appear significantly brighter and shifted to higher frequencies than it intrinsically is (Urry & Padovani 1995).

Although the classical Unification Model treats AGN classification as fixed and purely geometry-driven, some AGNs have been observed to change their spectral type over time (Ricci & Trakhtenbrot 2023). These so-called "changing-look AGNs" demonstrate that a purely orientation-based interpretation, such as the Unification Model, cannot explain all observed phenomena. They suggest that intrinsic changes, such as variations in accretion rate or obscuring material, can also affect the classification (Ricci & Trakhtenbrot 2023).
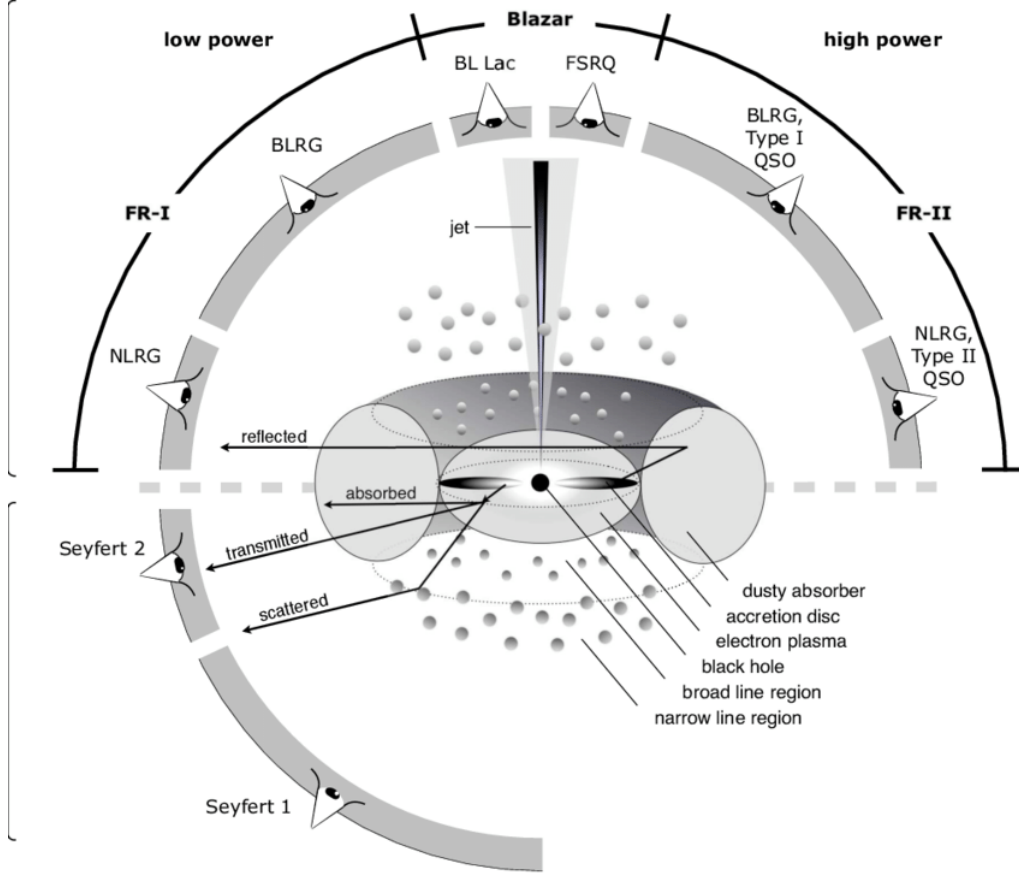
Figure 2.3: This graphic shows a schematic of the unification model of an AGN. The figure was adopted from (Beckmann & Shrader 2013).

2.1.4 Variability

The variability of active galactic nuclei (AGNs) is one of the key aspects that enables the study of their central regions, which generally cannot be probed with conventional spatially resolved observations. Variability is observed on timescales ranging from hours to several years and is generally stochastic, resulting in flux variations of both emission lines and continuum emission of up to a few tens of percent in the UV and optical bands (Ulrich et al. 1997; Ochmann et al. 2024). Although the origin of this variability is not yet fully understood, the most widely accepted models attribute it to inhomogeneities and instabilities within the accretion disk (Ulrich et al. 1997; Dexter & Agol 2010).

Depending on the underlying physical process, variations occur on different characteristic timescales. Processes such as thermal fluctuations or changes in the accretion flow happen on timescales of decades to centuries for typical SMBH masses and radii, and are therefore difficult to observe directly. In contrast, processes operating on shorter timescales are easier to study. Examples include gas motions and me-

chanical instabilities (e.g., sound waves) within the disk, which occur on timescales of weeks to months (Ricci & Trakhtenbrot 2023). The shortest timescale is the light-crossing timescale, $t_{\text{lc}} = R/c$, which specifies how long light takes to traverse the emitting region (e.g., the broad-line region, BLR) (Ricci & Trakhtenbrot 2023). Here, c denotes the speed of light, and R denotes the characteristic size or radius of the variable emitting region. Following Ricci & Trakhtenbrot 2023, assuming a SMBH of mass $\approx 10^8 \, M_\odot$, the light-crossing timescale can be written as

$$t_{\text{lc}} = \frac{R}{c} \simeq 0.87 \left(\frac{R}{150 \, r_g} \right) M_8 \, \text{days}, \tag{2.1}$$

where $r_g = GM/c^2$ is the gravitational radius of the black hole. Thus, the light-crossing timescale of the variable emitting region is of order days, and t_{lc} scales linearly with the size of the emitting region (Ricci & Trakhtenbrot 2023).

Because variations in the ionizing continuum occur on such short timescales, it is possible to measure delayed responses from other regions within the AGN that are correlated with the continuum, using long-term monitoring campaigns (Peterson 1997). In particular, the BLR responds to changes in the photoionizing continuum radiation of the central source with a time delay (lag) that is longer than the light-crossing timescale of the emitting region (Peterson 1997). This lag forms the basis of classical reverberation mapping, which will be further elaborated in the next section.

2.2 Reverberation Mapping

The main focus of this work is a classical reverberation mapping analysis of the broad lines of NGC 4593. Reverberation mapping probes the structure of the BLR around the SMBH by measuring the time delay (lag) between continuum variations and the correlated response of the broad lines. This lag can be used to constrain the BLR geometry and to estimate the SMBH mass (Cackett et al. 2018).

2.2.1 Principle of Reverberation Mapping

The fundamental assumption in reverberation mapping is that variations in the observed continuum flux are echoed by variations in the emission-line flux, with a measurable time delay (lag). When the continuum luminosity varies, the emission-line response follows with a measurable time lag (Cackett et al. 2021). The time lag τ corresponds to the average light-travel time between the photoionizing continuum source and the line-emitting regions. Assuming an idealized BLR consisting of spherically distributed clouds (Goad et al. 2012), then τ can be written as (Peterson
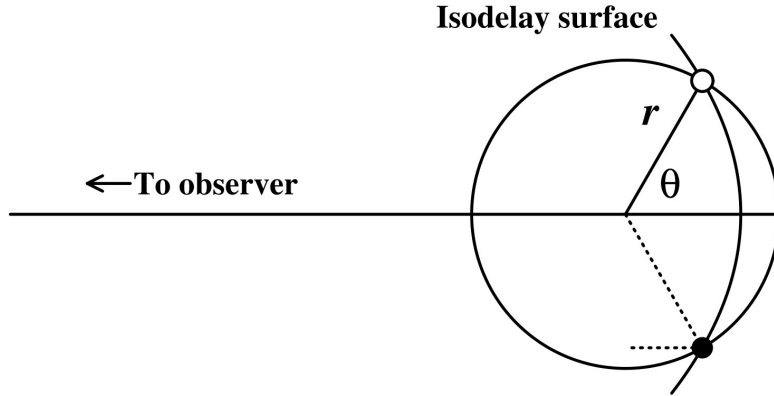
Figure 2.4: Spherical BLR model and an isodelay surface, adopted from (Peterson & Horne 2004).

1997)

$$\tau = (1 + \cos\theta) \cdot \frac{R_{\mathrm{BLR}}}{c}, \tag{2.2}$$

where R_{BLR} is the characteristic BLR radius, c is the speed of light, and θ is the angle between the line of sight and the position vector of the emitting gas with respect to the central source (see Figure 2.4) (Peterson 1997). The circle in Figure 2.4 represents the BLR modeled as spherical distribution of the clouds. For a fixed lag τ, the emitting regions that respond at that delay lie on a paraboloid aligned with the observer's line of sight, known as an isodelay surface. Therefore, emission observed at a given lag τ originates from the intersection of the BLR distribution with the corresponding isodelay surface (Peterson 1997). Thus, reverberation mapping can be used to "map" the BLR by inferring a characteristic BLR radius from the measured time lag (Peterson 1997). However, the observer receives emission from a range of delays (i.e., effectively from many isodelay surfaces), so the so-called transfer equation is required, which integrates over all delays (Peterson 1997):

$$L(t) = \int \Psi(\tau) C(t - \tau) d\tau. \tag{2.3}$$

Here, $\Psi(\tau)$ is the transfer function, which encodes the BLR geometry and kinematics, $C(t)$ is the continuum light curve, and $L(t)$ is the emission-line light curve (Peterson 1997). Although the BLR response is, in principle, fully described by the transfer function $\Psi(\tau)$, the lag is commonly estimated using cross-correlation techniques. In practice, recovering the full transfer function $\Psi(\tau)$ requires densely sampled, high signal-to-noise light curves spanning a duration much longer than the expected lag. Since real monitoring campaigns are often affected by observational gaps and noise, such reconstructions are rarely possible (Horne et al. 2004; Peterson

1993). For this reason, this project focuses on measuring the mean time lag between continuum and emission-line variations using the interpolated cross-correlation function (ICCF) method (Gaskell & Peterson 1987).

2.2.2 Lag Measurement

Using the notation of Peterson 1997, the cross-correlation function between the ionizing continuum and an emission line is defined as

$$F_{\text{CCF}}(\tau) = \int_{-\infty}^{\infty} L(t)C(t-\tau)dt. \tag{2.4}$$

The auto-correlation function of the ionizing continuum is

$$F_{\text{ACF}}(\tau) = \int_{-\infty}^{\infty} C(t)C(t-\tau)dt. \tag{2.5}$$

Together with the transfer equation (Equation 2.3), the cross-correlation function can be written as the convolution of the transfer function and the auto-correlation function of the ionizing continuum:

$$F_{\text{CCF}}(\tau) = \int_{-\infty}^{\infty} \Psi(\tau')F_{\text{ACF}}(\tau-\tau')d\tau'. \tag{2.6}$$

The lag is commonly defined as either the peak location (τ_{peak}) or the centroid (τ_{centroid}) of the CCF (Peterson 1997). While τ_{peak} is defined as the location of the CCF maximum, τ_{centroid} is calculated over all CCF points above a selected threshold, typically 80% of the peak value. Because the CCF is closely related to the transfer function, it is possible to infer a characteristic BLR size associated with the emission-line response (Peterson 1997), which can be expressed as

$$R_{\text{BLR}} = c \cdot \tau_{\text{centroid}}. \tag{2.7}$$

This follows from the light-travel timescale (Peterson et al. 2004). Since the centroid lag is generally considered a more robust estimator of the mean BLR light-travel time of the BLR (Peterson et al. 2004), it is used in this project.

The uncertainty of the measured lag is estimated using a Monte Carlo approach combining flux randomization (FR) and random subset selection (RSS) (Peterson et al. 1998; Peterson et al. 2004). In the FR step, each flux value is randomly perturbed according to its measurement uncertainty. In the RSS step, N data points are drawn randomly with replacement, while duplicate selections are discarded, resulting in a

new light curve with $M \leq N$ points. For each realization, the ICCF analysis is repeated, yielding a distribution of centroid lags. The uncertainties are estimated from the distribution of centroid lags obtained from the simulations (Peterson et al. 2004). The 16th and 84th percentiles of this distribution are adopted as the bounds of the 1σ confidence interval (Peterson et al. 1998).

2.2.3 Black Hole Mass

The reverberation mapping method can be used not only to measure the characteristic size of the BLR, but also to estimate the mass of the central SMBH. Under the assumption that the gas dynamics in the BLR are dominated by the gravitational potential of the central SMBH, the black hole mass can be estimated using the virial theorem (Peterson et al. 2004).

The centroid time lag τ_{centroid} provides an estimate of the characteristic BLR radius via Equation 2.7. Together with the velocity dispersion ΔV of the BLR gas, the virial mass is given by

$$M_{\mathrm{vir}} = \frac{R_{\mathrm{BLR}}\,\Delta V^2}{G}. \tag{2.8}$$

The black hole mass is then given by

$$M_{\mathrm{BH}} = f \cdot M_{\mathrm{vir}}. \tag{2.9}$$

Here, G denotes the gravitational constant, and f is a scale factor that accounts for the unknown geometry, kinematics, and inclination of the BLR (Peterson et al. 2004).The velocity dispersion ΔV can be estimated from the widths of the broad emission lines (Peterson et al. 2004).

The scale factor f is calibrated by matching reverberation-based black hole masses to the empirical $M_{\mathrm{BH}} - \sigma_*$ relation observed in inactive galaxies, where σ_* denotes the stellar velocity dispersion of the galactic bulge (Onken et al. 2004). Different studies have reported values of f based on various AGN samples, for example, $f = 5.5$ (Onken et al. 2004), $f = 4.31$ (Grier et al. 2013), and $f = 3.6$ (Graham et al. 2011).

The calibration of the scale factor also depends on the measurement method used for the line width of the broad emission lines (Peterson et al. 2004). Two commonly used measures are the line dispersion σ_{line} (see (Peterson et al. 2004)) and the FWHM. In this project, the FWHM is used as the line-width measure.

Following Probst et al. 2025, we adopt a scale factor of $f = 1.8$. This value is obtained by applying the relation $\mathrm{FWHM}/\sigma_{\mathrm{line}} \approx 2$ from Peterson et al. 2004 to the scale factor reported by Graham et al. 2011.

2.3   Bowen Fluorescence of OIλ8446

Previous studies of NGC 4593 report strong emission in the low-ionization lines O I λ8446 and the Ca II λ8498 λ8542 λ8662 triplet (Ochmann et al. 2025). In particular, O I λ8446 is of interest because it can be enhanced through a fluorescence mechanism referred to as Bowen fluorescence (Grandi 1980). The mechanism was first described by I.S. Bowen in 1934 to explain unexpected emission lines in nebular spectra. This mechanism describes a resonant line-pumping process in which photons emitted by one ion are absorbed by another ion of a different species via a permitted transition enabled by a near coincidence in wavelength between the pumping line and the absorbing transition. The resulting de-excitation leads to an enhancement of the emission lines (Bowen 1934).

One transition that can be enhanced by Bowen fluorescence is O I λ8446, which can be pumped by Lyβ photons (Netzer & Penston 1976). In this process, Lyβ photons at λ1025.72 Å are absorbed by neutral oxygen through the near-resonant transition $2p^4\,^3P_2 \rightarrow 3d\,^3D^0$ of O I at λ1025.77 Å. The excited $3d\,^3D^0$ level decays to $3p\,^3P$, which then decays to $3s\,^3S°$, emitting the O I λ8446 emission line (see figure 2.5) (Grandi 1980). This provides an additional excitation channel for O I λ8446, in addition to recombination.
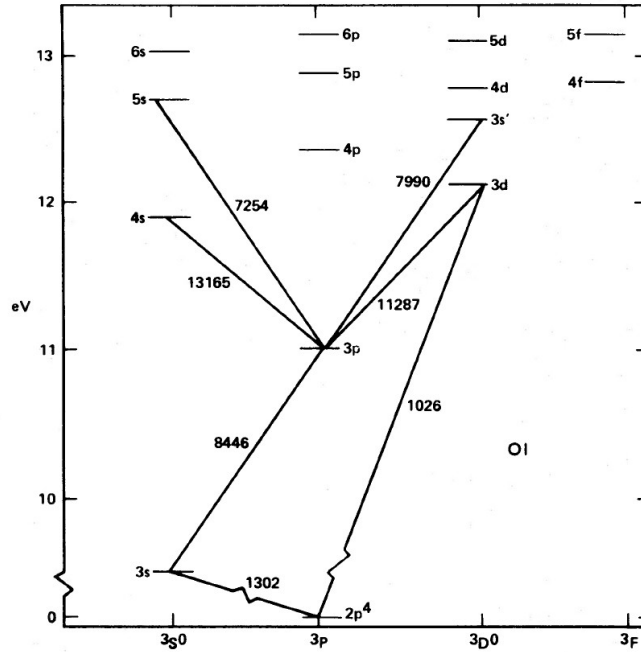

Figure 2.5: Energy level diagram displaying the process of Bowen fluorescence pumping of OI, adopted from (Grandi 1980).

3. Campaign and Data Preparation

The analysis of this campaign is based on the observation campaign of NGC4593 in 2016 by Cackett et al. 2018. This campaign took place between the 12th of July and the 6th of August with daily observations, which resulted in 26 successful out of 27 observations. It was performed with the Hubble Space Telescope (HST) using the Space Telescope Imaging Spectrograph (STIS) with the three different Gratings. The following section will cover an overview of the properties and specifications of NGC4593 and the campaign in 2016.

3.1 NGC4593

NGC 4593 is classified as a Seyfert 1 galaxy with a barred spiral morphology of type (R)SB(rs)b (Denney et al. 2006). It is located at RA $= 12^\mathrm{h}39^\mathrm{m}39.44^\mathrm{s}$, Dec $= -05°20'39.03''$ (J2000) and has a redshift of $z = 0.0083 \pm 0.0005$, corresponding to a distance of $\sim 35.9\,\mathrm{Mpc}$ (Koss et al. 2022) assuming a ΛCDM cosmology. The galaxy exhibits a prominent large-scale bar and nuclear dust ring connected to dust lanes along the bar, as seen in Figure 3.1.

The AGN in NGC 4593 exhibits strong broad emission lines, including Balmer and Lyman lines as well as He, O, and Ca lines among others (Kollatschny & Dietrich 1997; Cackett et al. 2018; Ochmann et al. 2025). Several variability and reverberation-mapping campaigns have monitored different broad emission lines, including Kollatschny & Dietrich 1997; Denney et al. 2006. They reported FWHM values from the mean (AVG) and root-mean-square (RMS) spectra of their respective campaigns. The RMS spectrum is defined as the standard deviation of the flux at each wavelength across epochs:

$$F_{\mathrm{RMS}}(\lambda) = \sqrt{\frac{1}{N-1} \sum_{i=1}^{N} \left[F_i(\lambda) - \bar{F}(\lambda) \right]^2}, \qquad (3.1)$$
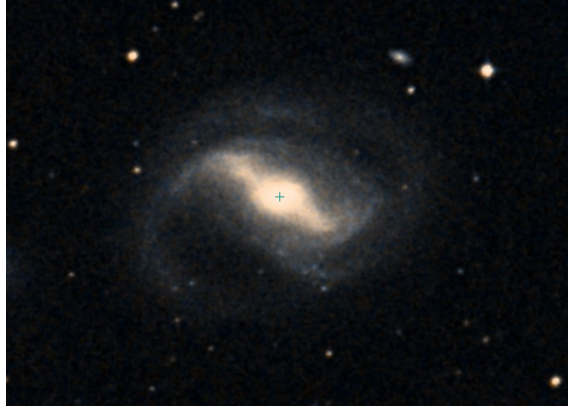
Figure 3.1: Screenshot of NGC 4593 visualized with Aladin Lite (*Aladin Lite* 2025) using DSS2 survey imagery (STScI 2025). The image is oriented with north up and east to the left. Right ascension increases to the left and declination increases upward.

with the mean spectrum at wavelength λ given by

$$\bar{F}(\lambda) = \frac{1}{N} \sum_{i=1}^{N} F_i(\lambda).$$ (3.2)

Kollatschny & Dietrich 1997 measured $\text{FWHM}_{\text{AVG/RMS}} = (3400 \pm 200)\,\text{km s}^{-1}$ for Hα, while Denney et al. 2006 reported for Hβ $\text{FWHM}_{\text{AVG}} = (5142 \pm 16)\,\text{km s}^{-1}$ and $\text{FWHM}_{\text{RMS}} = (4141 \pm 416)\,\text{km s}^{-1}$. Based on these broad-line widths, they estimated the SMBH mass to be $M \approx 1.4 \times 10^7\,M_\odot$ (Kollatschny & Dietrich 1997) and $M = (9.8 \pm 2.1) \times 10^6\,M_\odot$ (Denney et al. 2006). Overall, these results suggest that the SMBH mass is of order $10^7\,M_\odot$.

Furthermore, NGC 4593 shows a rare double-peaked emission-line complex involving O I $\lambda8446$ and the Ca II $\lambda8498$, $\lambda8542$, $\lambda8662$ triplet (Ochmann et al. 2025). Ochmann et al. 2025 found that the Ca II triplet has an intensity ratio of 1:1:1 and line profiles that closely resemble those of O I $\lambda8446$, exhibiting a red-to-blue peak ratio of 4:3 and a FWHM of $\approx 3700\,\text{km s}^{-1}$, suggesting that these lines originate in a similar high-density emission region.

3.2 The 2016 Hst Campaign

The campaign of Cackett et al. 2018 was designed to study wavelength-dependent continuum lags. It took place between the 12th of July and the 6th of August with daily observations, which resulted in 26 successful out of 27 observations. Observations were carried out with the Hubble Space Telescope (HST) using the Space Telescope Imaging Spectrograph (STIS) and three different gratings. The low-resolution

STIS gratings provided continuous spectral coverage over a broad wavelength range. In each observation, spectra were obtained using the G140L, G430L, and G750L. All spectra were acquired with the $52'' \times 0.2''$ slit.

The characteristics of the STIS gratings used in this work are summarized in Table 3.1. After standard pipeline processing, charge-transfer inefficiency (CTI) corrections were applied using an algorithm based on (Anderson & Bedin 2010). Remaining hot pixels were removed manually by interpolating the flux from neighboring pixels.

Table 3.1: Overview of STIS grating characteristics (Institute 2025).

Grating	Range [Å]	Exp. Time [s]	Res. Power	Dispersion [Å/pixel]
G140L	1119–1715	1234	~ 1000	0.6
G430L	2888–5697	298	$\sim 500 - 1000$	2.73
G750L	5245–10233	288	$\sim 500 - 1000$	4.92

3.3 Intercalibration and Determination of AVG and RMS Spectra

Reverberation mapping requires multiple epochs to capture variability. For the 2016 campaign of NGC 4593, we retrieved 27 spectra from the *Hubble Advanced Spectral Products (HASP)* 2025 archive using the HASP search form in *Mikulski Archive for Space Telescopes (MAST)* 2025 . 26 of these spectra are usable for further analysis. The top panel of Figure 3.2 shows all spectra in the spectral range from 4000Å to 9000Å.

For the subsequent analysis, the average spectrum (AVG) is obtained by averaging over all epochs, improving the signal-to-noise ratio (S/N). Furthermore it is essential for the reverberation mapping analysis to identify variability between the epochs, which can be assessed with the root-mean-spuare (RMS) spectrum, defined as the standard deviation of the flux at each wavelength across epochs (see. Equation 3.1). Constant features, such as narrow emission lines, vanish in the RMS spectrum, leaving only variable components such as broad emission lines. The top panel of Figure 3.2 shows the AVG and RMS spectra from the original retrieved data. Residual variability is still noticeable in nominally non-varying lines, particularly in the forbidden line [O III] $\lambda5007$. This indicates small wavelength misalignment between epochs. Therefore, an intercalibration anchored to the narrow [O III] $\lambda5007$ line was performed. This was achieved by shifting the wavelengths of the individual spectra and

scaling the line flux to a constant value. As a narrow line, the flux of [O III] $\lambda5007$ can be assumed to remain constant over the timescale of the campaign. Based on this assumption, the flux of each spectrum was scaled to $(106 \pm 5) \times 10^{-15}\,\mathrm{erg\,s^{-1}\,cm^{-2}}$ and the wavelength was shifted by a maximum of 1Å.

Figures 3.2 shows a comparison of the original and the intercalibrated epochs and the corresponding AVG and RMS spectra. The disappearance of narrow features in the calibrated RMS spectrum, especially the [O III] $\lambda5007$ line, confirms that the apparent variability in the RMS of the original epochs was induced by the wavelength shifts between them, rather than intrinsic line variability. However the intercalibration was only applied to the optical part of the spectra due to its limited reliability. In the following analysis, the intercalibrated AVG and RMS spectra are used for the optical range obtained with the G430L and G750L gratings, while the AVG and RMS spectra from the original epochs are used for the UV emission-line analysis, as these were acquired with the G140L grating.
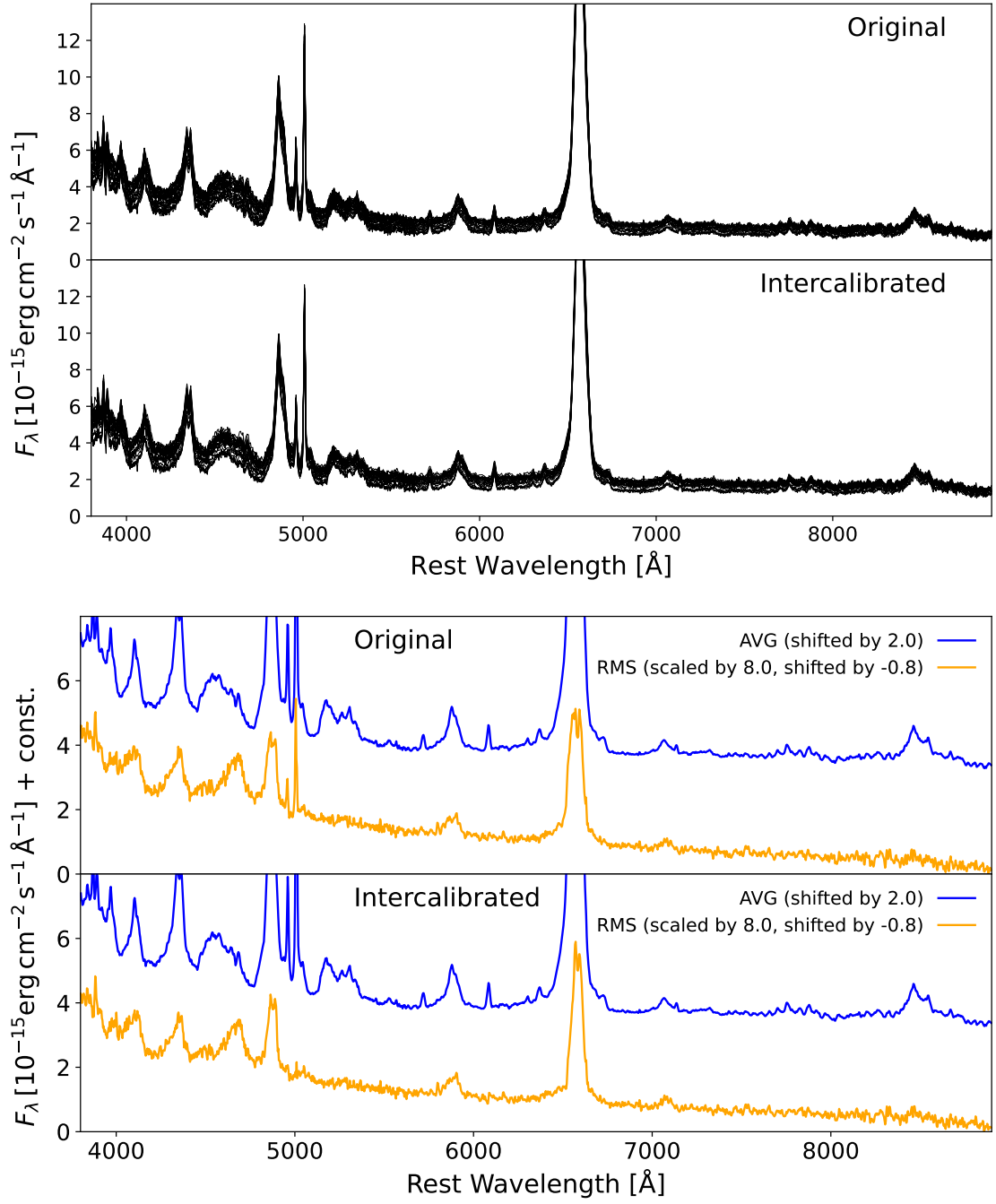
Figure 3.2: Comparison of the spectral range between 4000Å and 9000Å from the 2016 HST campaign of NGC 4593, showing the effects of [O III] $\lambda 5007$ intercalibration on both the individual spectra (top) and the derived average and rms spectra (bottom).

4. Reverberation Mapping Analysis of NGC4593

4.1 Line Identification

Having obtained the AVG- and RMS spectrum of NGC4593, the next step is the identification of the emission lines. Figures 4.1 and 4.2 show the optical to near-infrared range between 3900Å and 9000Å and the UV range between 1100Å and 1700Å, respectively. Looking at Figure 4.1, the most prominent broad emission lines

Figure 4.1: Optical-to-NIR AVG and RMS spectrum with identified emission lines.

in the AVG spectrum are the Balmer-Lines, with Hα being the strongest followed by Hβ and Hγ. Their variations are clearly visible in the RMS spectrum and the line profiles of Hα and Hβ in particular show strong similarities, which will be

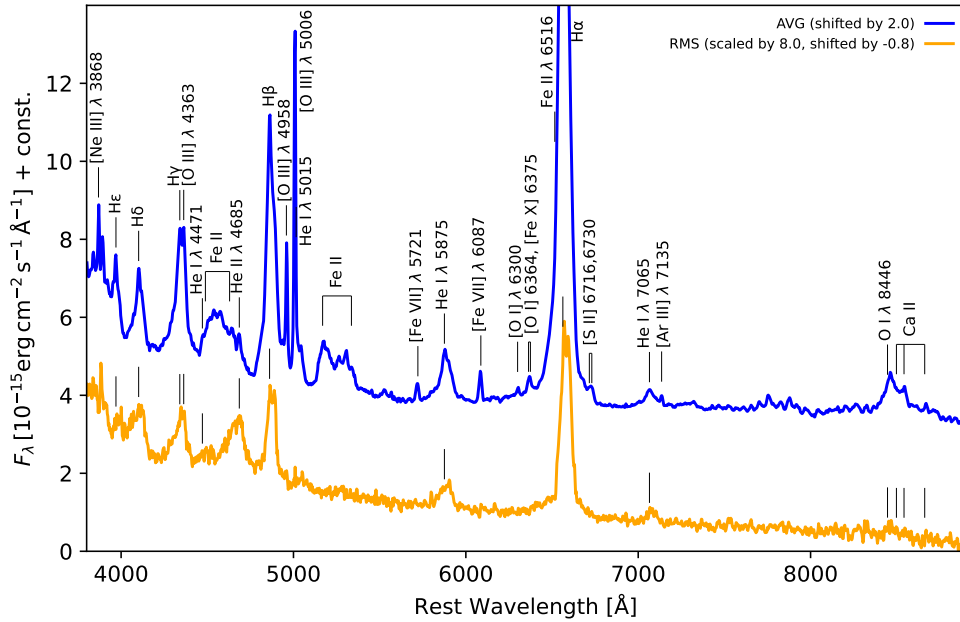discussed in more detail later in this chapter. In addition to the Balmer emission lines, several He-emission lines such as He II λ4685, He I λ5875 and He I λ7065 show variability. Another significant broad emission line complex appears in the NIR part of the spectrum, including the O I λ8446 and Ca II lines. The O I λ8446 line is of particular interest in this thesis, as it shows variability that has never been measured using reverberation mapping before.

Apart from the broad emission lines, the AVG spectrum also exhibits several strong forbidden emission lines with the [O III] λ5007 and the [O III] λ4958 as the most prominent ones. As mentioned in the previous chapter, the first one was used for the intercalibration of the spectra and, as expected, shows no variability in the RMS spectrum, similar to the other forbidden lines. Finally, the AVG spectrum shows additionally two Fe II emission line groups, that shows no variation in the RMS spectrum. The UV spectrum shown in Figure 4.2 contains both broad and semi-
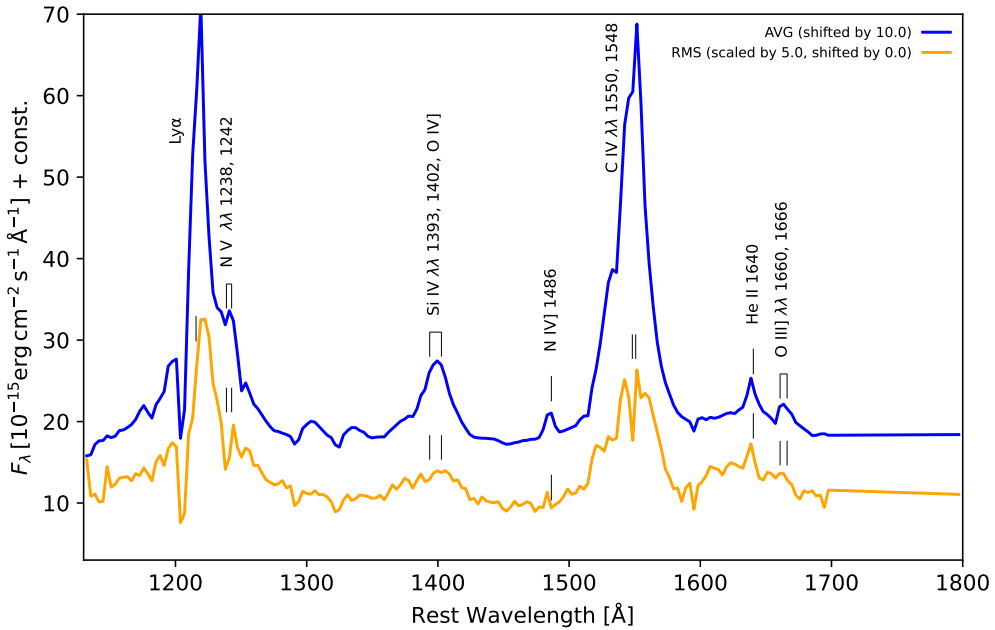
Figure 4.2: UV spectrum AVG and RMS spectrum with identified emission lines

forbidden emission lines. In addition to the prominent Si and C broad emission lines, it shows strong and variable Lyα emission, which is of particular significance for this thesis.

The Bowen fluorescence of O I λ8446, which is investigated in this analysis, is typical driven by the emission of the Lyβ line (Grandi 1980), which lies outside the spectral range of the HST Campaign. However, as can be seen in figure 4.2, Lyα still lies in the spectral range of the campaign, as the bluest broad line of the taken spectra.

As Lyα and Lyβ are assumed to originate in the same physical region, Ly$_\alpha$ can be used to examine the corelation of O I $\lambda 8446$ and Lyα for Bowen fluorescence.

4.2   Emission Line and Continua Measurement

After identifying the emission lines, the next step of the analysis is to calculate the fluxes of those lines. This is done with the help of a python-based tool called GECHO created by M. Probst. It enables to import full campaigns, determine the AVG and RMS spectra, extracting lightcurves and do further measurments, like e.g. ICCF methode to measure lags and line-wifth measurments (Gaskell & Peterson 1987; Peterson et al. 2004), which will be further discussed in Section 4.5
With help of GECHO the flux density gets integrated over the extent of each emission line for every observed spectrum of the campaign. Here it is important to define the integration limits so that all of the emission line flux is measured in this way. To ensure this, a parallel view of the AVG- and RMS-spectrum was used to define those integration limits, and to ensured, that no component of any other line is contributing to the line flux of the measured line. But before the line flux can be calculated, the surrounding continuum has to be subtracted, which can be done by interpolating a linear underlying continuum between sections on the blue and red side with no line contribution. The chosen integration limits and pseudo-continua can be found in Table 4.1. With the fluxes of each line now derived from all observed spectra, it is possible to extract the lightcurves of the measured emission line, which will be further covered in the next section.
Besides the emission line lightcurves, continua lightcurves from different wavelength ranges are required for the further analysis. The extraction process is similar to the emission line lightcurves, except that they get calculated by the mean flux density of a sufficiently large region without line emission or absorption. Therefore, no pseudo-continuum subtraction is necessary. The chosen integration limits for the continua can be found in Table 4.2.

4.2.1   Variability Statistics and Uncertainties estimation

To quantify the variability of the emission lines and continua variability statistics, defined by Rodriguez-Pascual et al. 1997 gets adopted. This definition includes the extrema of the emission line flux densities as well as the extrema of the integrated continuum fluxes, $F_{\min}$ and $F_{\max}$, the maximum-to-minimum flux ratio $R_{\max}$, the mean flux $\langle F \rangle$, the standard deviation σ_F, and finally the fractional variability,

Table 4.1: Integration Limits and Pseudo-Continua of the measured emission lines

Line	Integration Limits [Å]	Pseudo-Continua [Å]
Lyα	$1207 - 1238$	$1151 - 1161, 1462 - 1468$
Hα	$6520 - 6634$	$6107 - 6129, 6861 - 6900$
Hβ	$4828 - 4924$	$4762 - 4774, 5085 - 5112$
Hγ	$4317 - 4391$	$4197 - 4220, 4435 - 4450$
HeI $\lambda 5875$	$5840 - 5941$	$5645 - 5653, 6044 - 6057$
HeII $\lambda 4685$	$4610 - 4744$	$4435 - 4450, 4762 - 4774$
OI $\lambda 8446$	$8380 - 8498$	$8005 - 8031, 8850 - 8955$
OIII $\lambda 5007$	$4982 - 5033$	$4762 - 4774, 5085 - 5112$

Table 4.2: Integration Limits of the measured continua

Line	Integration Limits [Å]
Cont. 1150	$1151 - 1161$
Cont. 4010	$4026 - 4033$
Cont. 4440	$4435 - 4450$
Cont. 5100	$5085 - 5112$
Cont. 6110	$6107 - 6129$
Cont. 6880	$6861 - 6900$
Cont. 8015	$8005 - 8031$
Cont. 8900	$8864 - 8955$

which is defined as:

$$F_{\text{var}} = \frac{\sqrt{\sigma_F^2 - \Delta^2}}{\langle F \rangle} \tag{4.1}$$

Here Δ^2 is the mean square value of the uncertainties of the fluxes defined as:

$$\Delta^2 = \frac{1}{N} \sum_{i=1}^{N} \Delta_i^2 \tag{4.2}$$

The results of these parameters can be found in Table 4.3.

The uncertainties of the continuum and emission-line lightcurves are estimated from two components. The first component originates from the noise in the flux densities over the pixels within the integration bounds, N_{pixel}. For the continuum lightcurves, the noise uncertainty is estimated as

$$\sigma_{\text{noise}}^{\text{cont}} = \frac{\sigma_F}{\sqrt{N_{\text{pixel}}^{\text{cont}}}}, \tag{4.3}$$

where σ_F denotes the standard deviation of the flux density within the selected continuum window. Since the emission-line lightcurves are extracted by integrating the

continuum-subtracted flux density, the corresponding noise uncertainty is estimated using the noise measured from the used pseudo-continua, $\sigma_{\mathrm{noise}}^{\mathrm{p.cont.}}$:

$$\sigma_{\mathrm{noise}}^{\mathrm{lines}} = \frac{\sigma_{\mathrm{noise}}^{\mathrm{p.cont.}} \cdot \Delta\lambda}{\sqrt{N_{\mathrm{pixel}}^{\mathrm{line}}}}. \tag{4.4}$$

Here, $\Delta\lambda$ denotes the integration window used for the emission line, and $N_{\mathrm{pixel}}^{\mathrm{line}}$ denotes the number of pixels within this window.

The second component originates from the intercalibration of the epochs of the campaign. The flux of each epoch is scaled based on the narrow emission line [O III] $\lambda5007$, which is assumed to be constant over the campaign. To account for the systematic uncertainty introduced by the intercalibration, the fractional variability of [O III] $\lambda5007$ is multiplied by the integrated flux values f_i and used as a proxy for the intercalibration uncertainty:

$$\sigma_i^{\mathrm{cal.}} = F_{\mathrm{var}}^{[\mathrm{O\,III}]\,\lambda5007} \cdot f_i. \tag{4.5}$$

This yields the total light-curve uncertainty:

$$\sigma_i = \sqrt{\left(\sigma_i^{\mathrm{cal.}}\right)^2 + \left(\sigma_{\mathrm{noise}}\right)^2}, \tag{4.6}$$

where σ_{noise} corresponds to $\sigma_{\mathrm{noise}}^{\mathrm{cont}}$ for continuum light curves and to $\sigma_{\mathrm{noise}}^{\mathrm{lines}}$ for emission-line light curves.

4.3 Lightcurves

The variability of the lightcurves can be seen in the visualization of the lightcurves in Figure 4.3 and 4.4. In addition to the measured lightcurves of the HST campaign, the UVOT UVW2 lightcurve taken with SWIFT by McHardy et al. 2018 is displayed for comparison which shows a higher sample-size that the lightcurves of the HST campaign. Its central wavelength is located at about 1930 Å (McHardy et al. 2018) and was used as a reference lightcurve in Cackett et al. 2018 as well, which makes is interesting as a reference lightcurve for this analysis too.

Looking at the continuum lightcurves in Figure 4.3 they show a broadly similar overall shape. All lightcurves begin at the highest flux level in most cases, except for UVW2, whose peaks have comparable heights throughout, and the 1150 continuum, which reaches its highest flux at the second maximum. The initial maximum is followed by a pronounced flux minimum, with a decrease of about 25–46% relative

Table 4.3: Variability statistics of the measured continua and broad lines with minimum (2) and maximum flux density or integrated flux (3), peak-to-peak ratio (4), mean (5), standard deviation (6) and fractional variation (7).

Continuum/Line	$F_{\min}$	$F_{\max}$	$R_{\max}$	$\langle F \rangle$	σ_F	F_{var}
(1)	(2)	(3)	(4)	(5)	(6)	(7)
Cont. 1150	0.52	1.35	2.58	0.86	0.25	0.28
Cont. 4010	2.68	4.21	1.57	3.49	0.47	0.14
Cont. 4440	2.42	3.73	1.54	3.14	0.39	0.12
Cont. 5600	1.36	2.15	1.59	1.82	0.25	0.14
Cont. 6110	1.49	2.27	1.53	1.9	0.23	0.12
Cont. 6880	1.33	2.01	1.5	1.72	0.2	0.11
Cont. 8015	1.18	1.69	1.43	1.48	0.15	0.1
Cont. 8900	1.14	1.52	1.33	1.38	0.11	0.08
Lyα	66.87	94.88	1.42	82.21	8.03	0.1
Hα	112.34	129.72	1.15	122.03	4.36	0.04
Hβ	32.7	39.12	1.2	36.49	1.77	0.05
Hγ	14.45	17.85	1.24	16.5	0.94	0.06
HeII $\lambda4685$	5.53	9.81	1.77	7.73	1.37	0.18
HeI $\lambda5875$	6.81	9.54	1.4	8.49	0.62	0.07
OI $\lambda8446$	7.47	9.13	1.22	8.32	0.37	0.04

to the overall maximum flux of each curve. Subsequently, the light curves rise again toward another peak, which is more distinct in the UV and blue continua and is followed by another drop in flux. While all continua except Cont. 4010 exhibit an additional another local maximum, the flux then decline steadily toward a global minimum near the end of the campaign.

For the RM analysis the real distance between the SMBH and the BLR is of most interests. Assuming that the continuum radiation originate from the accretion disk it is common to use the bluest available continuum band, which is expected to originate closest to the SMBH, which would be the continuum around 1150 Å. But because the higher sample rate, the UVW2 continuum was selected as the main reference lightcurve for the further analysis.

Looking now at the emission-line lightcurves in Figure 4.4 correlation between them and the UVW2 continuum can already be spotted. The three major features of the UVW2 lightcurve, the first strong minimum, the two maxima in the center and the strong drop at the end, can be also identified in the emission line lightcurves with respective shifts in time, which will be further investigated in Section 4.5.
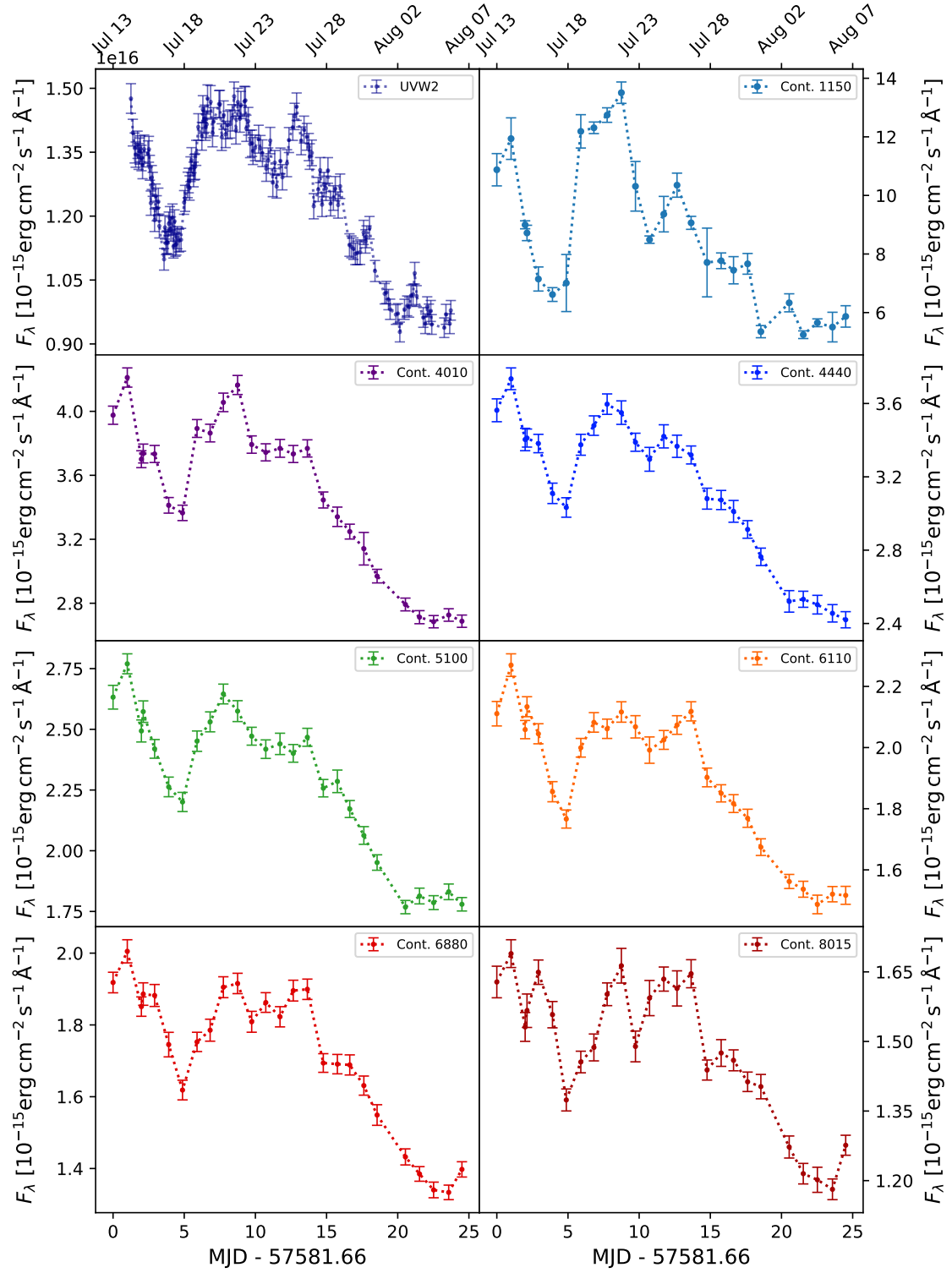
Figure 4.3: Comparison of the continua lightcurves. The first panel shows the UVW2 continuum lightcurve obtained from McHardy et al. 2018, while the other panels show the measured continua defined in Table 4.2
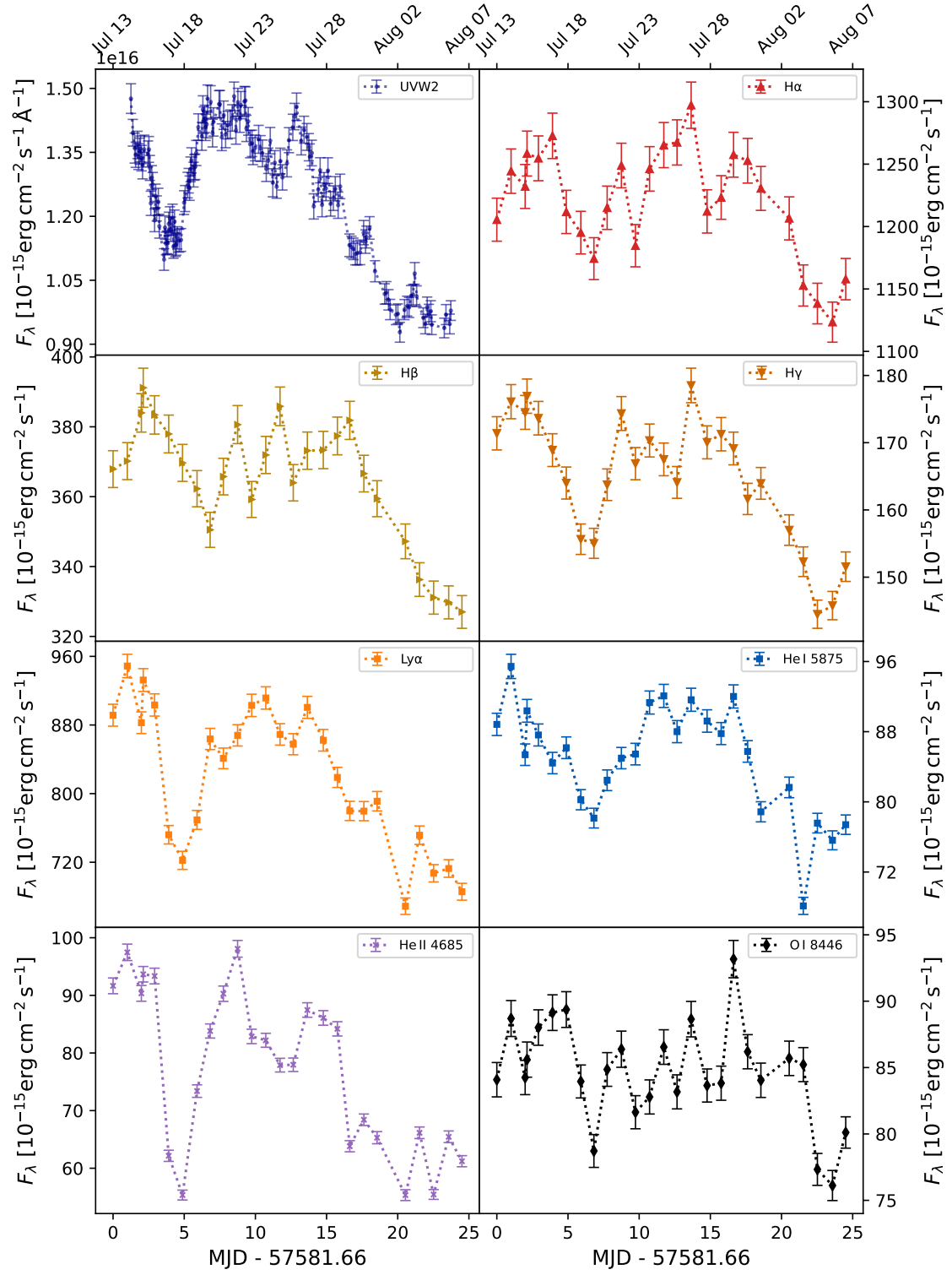
Figure 4.4: Comparison of the emission-line lightcurves to the UVW2 reference lightcurve in the first panel. The UVW2 lightcurve was obtained from McHardy et al. 2018

4.4 Line Profiles

In addition to the variability, it is possible to investigate the kinematics of the BLR by extracting the line profiles of broad emission lines and investigating their shape and line width. Following the same procedure as for the lightcurve extraction, an underlying linear continuum is interpolated using a chosen blue and red pseudo-continuum for each line in both the AVG and RMS spectra. The selected boundaries of the pseudo-continua are listed in Table 4.4. This interpolated continuum is subtracted to define a zero-flux baseline for each line profile and to allow a better comparison.

Table 4.4: Bounderies of the blue and red pseudo-continua used for the interpolation of underlying continua for line profile extraction.

Line	Pseudo-Continua AVG [Å]	Pseudo-Continua RMS [Å]
Hα	$6194 - 6216, 6861 - 6900$	$6279 - 6301, 6742 - 6781$
Hβ	$4762 - 4774, 5085 - 5112$	$4762 - 4774, 4967 - 4984$
Hγ	$4197 - 4220, 4435 - 4450$	$4197 - 4220, 4417 - 4429$
OI $\lambda 8446$	$7999 - 8025, 8775 - 8798$	$8222 - 8238, 8748 - 8767$
HeI $\lambda 5875$	$5679 - 5697, 6044 - 6057$	$5736 - 5753, 6027 - 6045$
HeII $\lambda 4685$	$4198 - 4225, 4762 - 4774$	$4543 - 4554, 4766 - 4778$

Subsequently, the line profile is converted to velocity space using

$$v_i = c \cdot \frac{(\lambda_i - \lambda_{\text{central}})}{\lambda_{\text{central}}}. \tag{4.7}$$

Here, λ_i denotes the wavelength values, λ_{central} the central wavelength of the emission line in rest-frame, and c the speed of light. The flux is normalized to the maximum of the emission lines. Figure 4.5 shows an overview of the extracted and normalized line profiles of Hα, Hβ, Hγ, O I $\lambda 8446$, He I $\lambda 5875$, and He II $\lambda 4685$ in both the AVG and RMS spectra. The Balmer lines and the helium lines show well-defined profiles in both AVG and RMS, making them suitable for further kinematic analysis. The O I $\lambda 8446$ profile is blended with the Ca II $\lambda 8498$ $\lambda 8542$ $\lambda 8662$ triplet in the AVG spectrum. Moreover, the RMS profile has low signal-to-noise, so this line is not considered further in the kinematic analysis.

After selecting the suitable broad emission lines, the FWHM of the normalized AVG and RMS profiles was calculated, which are listed in Table 4.5. The FWHM of the AVG profile of He II $\lambda 4685$ was not attempted to be calculated, as the blue wing is mostly overlapped by the Fe II band between 4489 Å and 4629 Å.
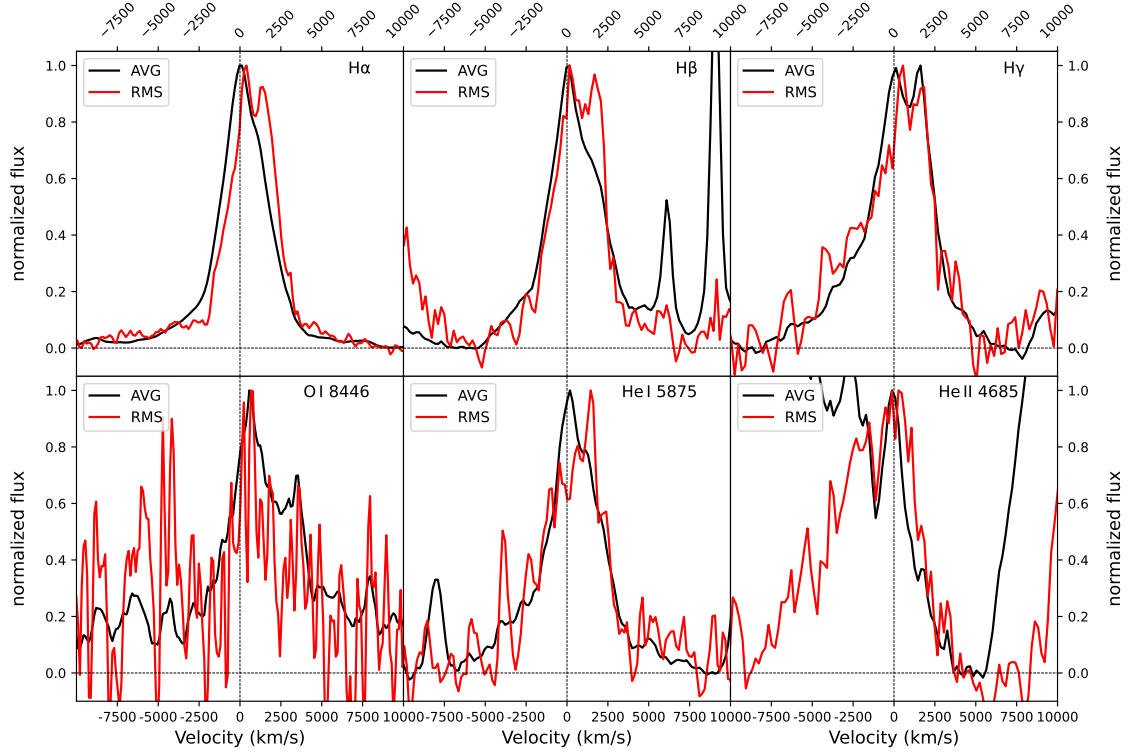
Figure 4.5: A plot of the AVG and RMS line profiles of the broad emission lines Hα, Hβ, Hγ, OI λ8446, HeI λ5875 and HeII λ4685.

Table 4.5: Measured FWHM and of the AVG and RMS line profiles.

Line	FWHM AVG[km/s]	FWHM RMS[km/s]
Hα	3038 ± 250	3090 ± 250
Hβ	3526 ± 200	3387 ± 200
Hγ	4014 ± 200	3794 ± 500
HeI λ5875	3369 ± 300	4235 ± 300
HeII λ4685	-	5881 ± 300

The uncertainties were estimated based on the instrumental dispersion of the grating, the shape and noise of the line profiles. Table 3.1 lists the gratings used for the different wavelength ranges. Hα and He I λ5875 were measured with the G750L grating with a dispersion of 4.97 Å/pixel, while Hβ, Hγ, and He II λ4685 were measured with the G430L grating with a dispersion of 2.73 Å/pixel. Using Equation 4.7 and the rest-frame central wavelengths of the emission lines, this corresponds to an equivalent dispersion of 222.9 and 249.1 km s^{-1} / pixel for Hα and He I λ5875, and 169.2, 189.4 and 175.7 km s^{-1} / pixel for Hβ, Hγ, and He II λ4685, respectively. The uncertainties for the FWHM of the AVG line profile and the RMS profiles of

Hα and Hβ were estimated based on these dispersion. For the RMS profiles of Hγ, He I λ5875 and He II λ4685 the uncertainties get estimated a bit higher, as they are more noisy than the other profiles.

4.4.1 Balmer-Lines

A comparison of the Balmer-line profiles Hα, Hβ, and Hγ is shown in Figure 4.6. With the exception of the AVG profile of Hγ, which is affected by the narrow [O III] λ4363 line overlapping the Hγ profile, the lines exhibit a similar asymmetric shape their AVG profiles. All three lines show a steep blue wing. Hα and Hβ exhibit nearly identical gradients, while Hγ is broader up to $\approx -1000\,\mathrm{km\,s^{-1}}$ before matching the slope of the other profiles. The red wings of Hα and Hβ are again similar, showing a bump at around $\approx 1000\,\mathrm{km\,s^{-1}}$ and $\approx 2500\,\mathrm{km\,s^{-1}}$, respectively, resulting in the asymmetric profile. Comparing the line widths, the FWHM values of the three profiles differ (see. Table 4.5). This can be attributed to the overlap with [O III] λ4363 in the case of Hγ and to additional narrow-line components of each line. Since these narrow components are hard to isolate in the profiles and vanish in the RMS spectra, no attempt was made to decompose the AVG profiles. Instead, the RMS line widths are adopted for the subsequent analysis.
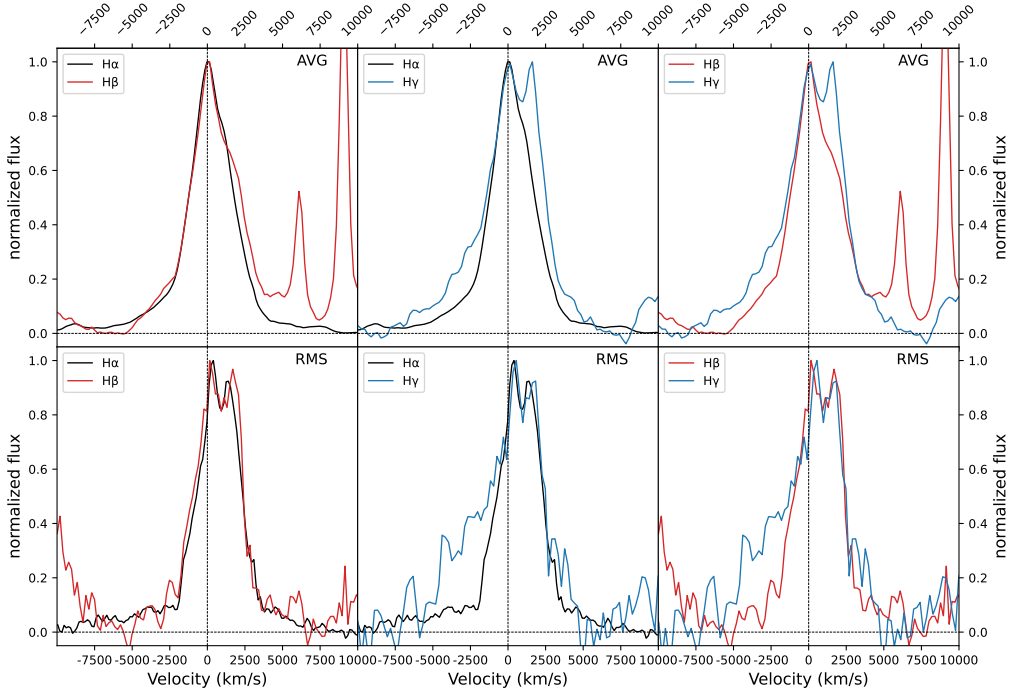

Figure 4.6: Comparison of the normalized AVG and RMS line profiles of the Balmer lines Hα vs Hβ and Hα vs Hγ in velocity space.

The RMS profiles of the Balmer lines show an asymmetric double-peaked shape. Again, the profiles of Hα and Hβ show a very similar shape, while the blue wing of Hγ is more extended and becomes noisy at higher velocities. Since the narrow components vanish in the RMS profiles, the red wing of Hγ becomes clearly visible and follows the shape of Hα and Hβ. The FWHM values of the three RMS profiles differ less than in the AVG case and lie within their uncertainties (see Table 4.5). For all three profiles, the double-peaked structure is red-shifted, with the blue peak located at $\approx 200\,\mathrm{km\,s^{-1}}$ and the red peak at $\approx 2000\,\mathrm{km\,s^{-1}}$. This indicates that the Balmer lines show a asymmetric variability distribution, with stronger flux variations in the red wing than in the blue wing.

4.4.2   Helium-Lines

Moving over to the Helium lines, Figure 4.7 shows a comparison of the AVG and RMS line profile of HeI $\lambda5875$ and HeII $\lambda4685$. The blue wing of the HeII $\lambda4685$ AVG profile is partly overlapped by the Fe II band between $4489\,\text{Å}$ and $4629\,\text{Å}$ at velocities above about $-1000\,\mathrm{km\,s^{-1}}$. While the visible part of its blue wing follows the same shape as the HeI $\lambda5875$ blue wing shape, the red wing of HeI $\lambda5875$ is much broader. Still, both red wings show a similar shape and an additional smaller peak at around $1000\,\mathrm{km\,s^{-1}}$. Since more than half of HeI $\lambda5875$ blue wing is overlapped by the Fe II band, a calculation of its FWHM was not attempted. Still, looking at the the line widths at 0.6 height of the line with $\approx 2500\,\mathrm{km\,s^{-1}}$ for HeI $\lambda5875$ and $\approx 1600\,\mathrm{km\,s^{-1}}$ for HeII $\lambda4685$, it can be assumed that HeI $\lambda5875$ show a much broader line profile in the AVG than HeII $\lambda4685$. Again this can result from underlying narrow-components, which is why the FWHM of the RMS profiles will be used for the subsequent analysis.

Other than in the AVG profile, HeI $\lambda5875$ now shows a smaller line width than HeII $\lambda4685$ and higher noise. Looking at the HeI $\lambda5875$ profile, its maximum is red-shifted to $\approx 2000\,\mathrm{km\,s^{-1}}$, while the maximum of the HeII $\lambda4685$ profile is located around $0\,\mathrm{km\,s^{-1}}$. Following that it HeI $\lambda5875$ shows more variation in its red wing than HeII $\lambda4685$ does. Still, it is possible to notice similarities in their shapes. The blue wing of HeI $\lambda5875$ extend up to about $\approx -5000\,\mathrm{km\,s^{-1}}$ and its red wing about $\approx 4000\,\mathrm{km\,s^{-1}}$ while HeII $\lambda4685$ blue wing extend up to about $\approx -9000\,\mathrm{km\,s^{-1}}$ its red wing about $\approx 5000\,\mathrm{km\,s^{-1}}$. Going from the maxima, it shows that both profiles show a much more extended blue wing and a very steep red wing.
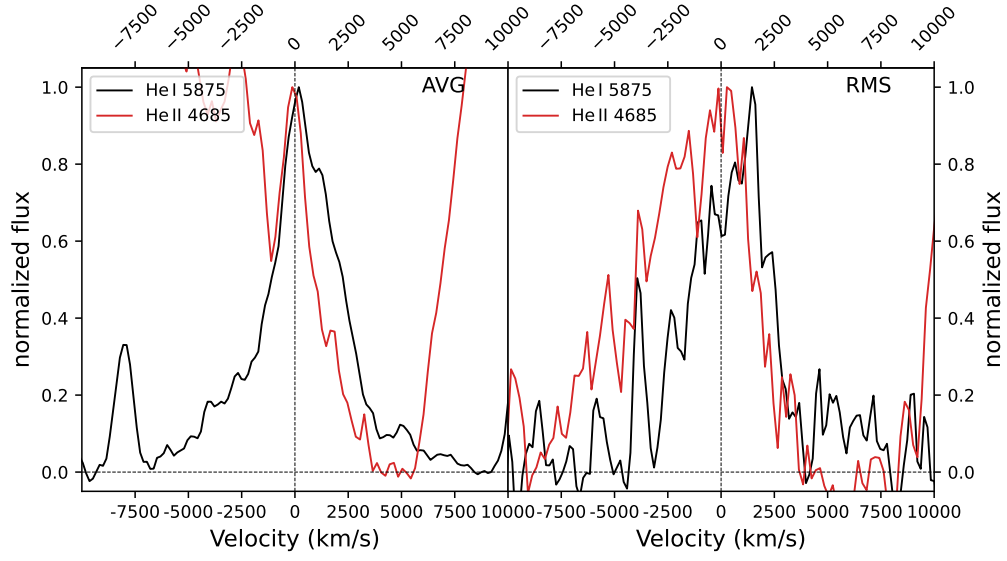
Figure 4.7: Comparison of the AVG and RMS line profiles of the Helium lines HeI $\lambda5875$ vs HeII $\lambda4685$.
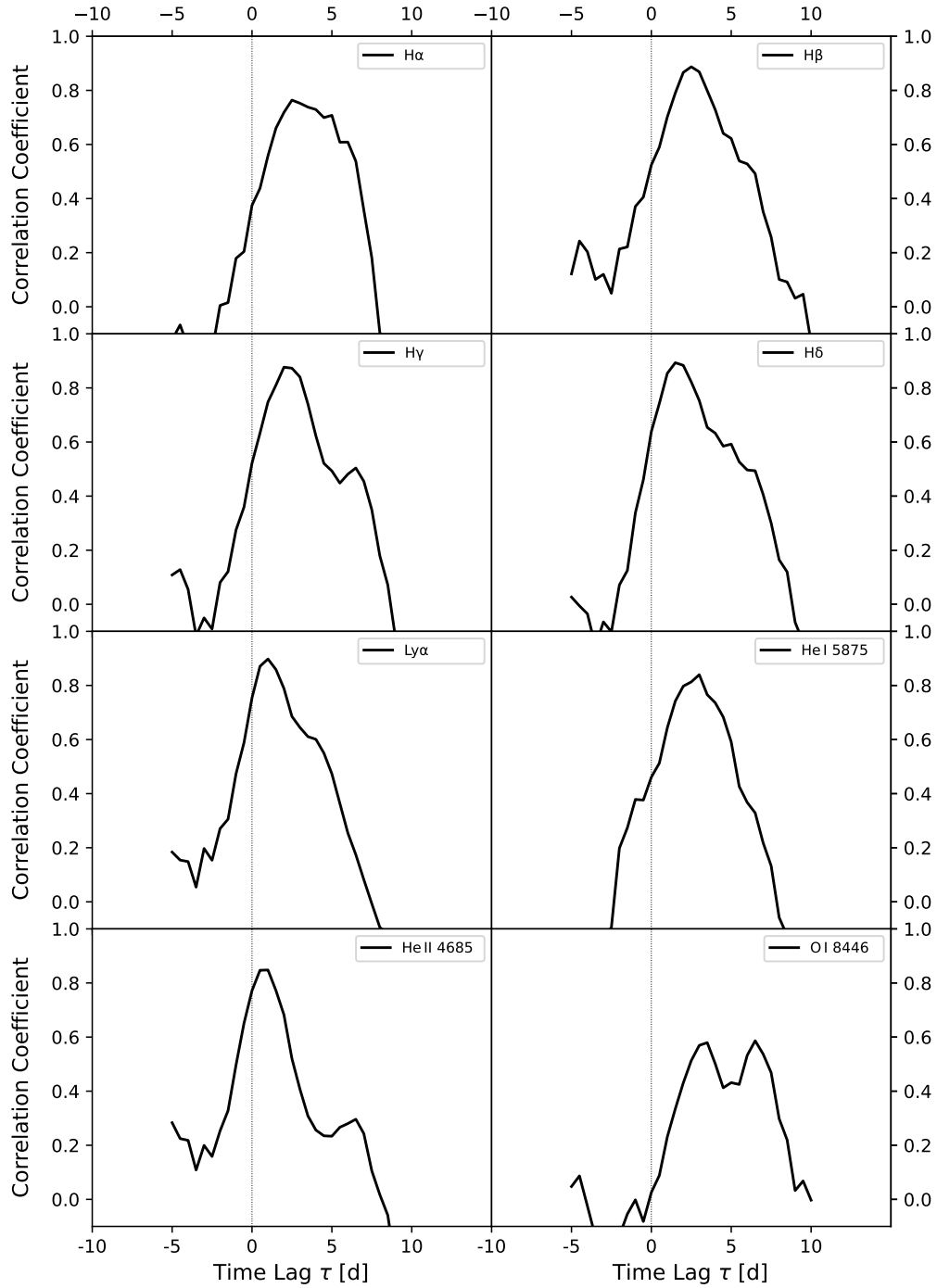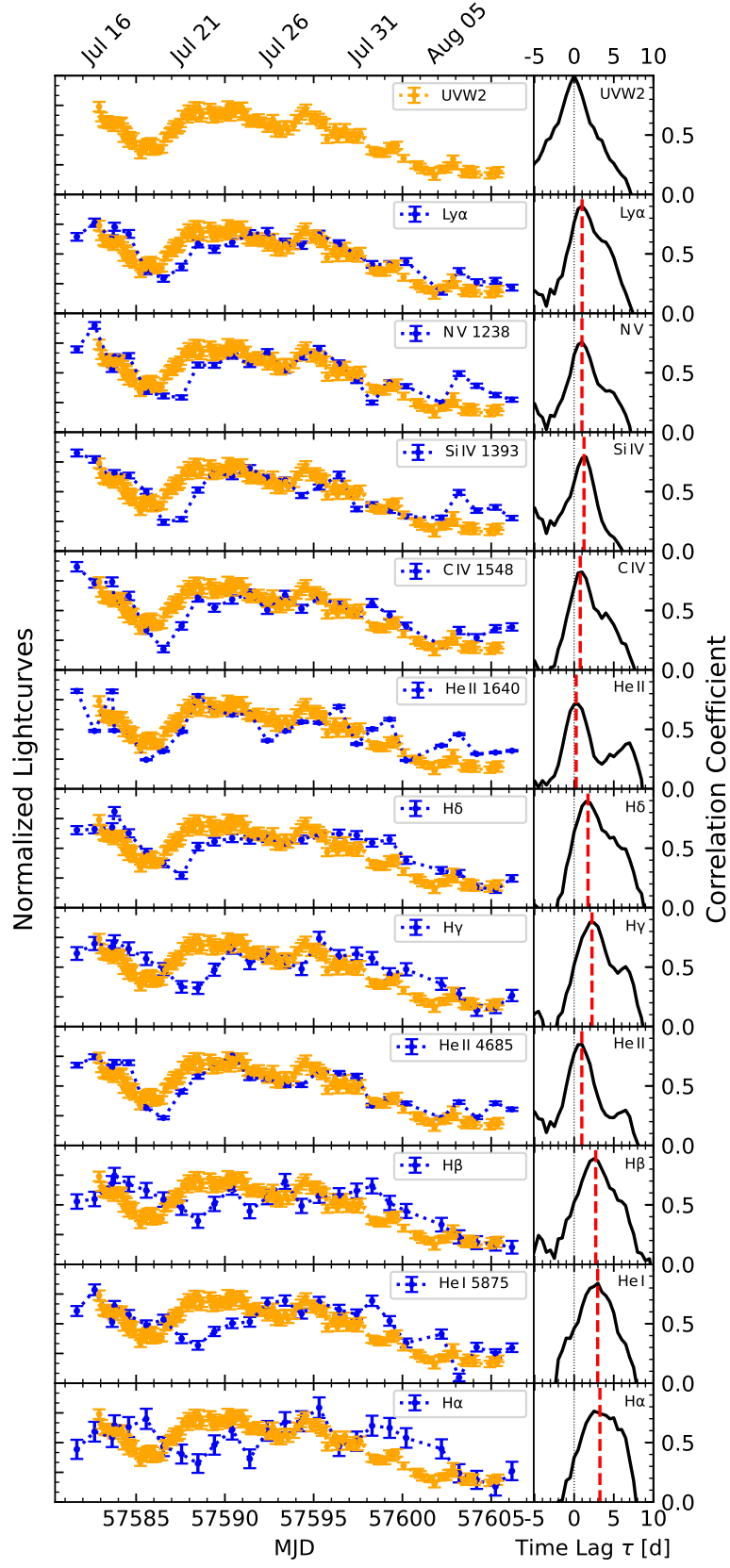
4.5 Time Lag and BH Masses

Figure 4.8: AVG RMS Spektrum

Figure 4.9: AVG RMS Spektrum

5. Discussion

Bibliography

Aladin Lite (2025). CDS (Centre de Données astronomiques de Strasbourg). URL: `https://aladin.cds.unistra.fr/AladinLite/` (visited on 07/19/2025).

Anderson, J. & L. R. Bedin 2010, *Publications of the Astronomical Society of the Pacific*, 122, 1035.

Antonucci, Robert 1993, *Annual Review of Astronomy and Astrophysics*, 31, 473–521.

Beckmann, Volker & Chris R. Shrader 2013, *The AGN phenomenon: open issues*, URL: `https://arxiv.org/abs/1302.1397`.

Bowen, I. S. 1934, *Publications of the Astronomical Society of the Pacific*, 46, 146–148.

Bowen, I. S. 1947, *Publications of the Astronomical Society of the Pacific*, 59, 196.

Cackett, E. M., M. C. Bentz, & E. Kara 2021, *iScience*, 24, 102557.

Cackett, E. M., C.-Y. Chiang, I. McHardy, et al. 2018, *The Astrophysical Journal*, 857, 53.

Denney, K. D., M. C. Bentz, B. M. Peterson, et al. 2006, *Astrophysical Journal Letters*, 653, 152–158.

Dexter, J. & E. Agol 2010, *The Astrophysical Journal*, 727, L24.

Gaskell, C. M. & B. M. Peterson 1987, *The Astrophysical Journal Supplement Series*, 65, 1.

Goad, M. R., K. T. Korista, & A. J. Ruff 2012, *Monthly Notices of the Royal Astronomical Society*, 426, 3086–3111.

Graham, A. W., C. A. Onken, E. Athanassoula, et al. 2011, *Monthly Notices of the Royal Astronomical Society*, 412, 2211–2228.

Grandi, S. A. 1980, *The Astrophysical Journal*, 238, 10.

Grier, C. J., P. Martini, L. C. Watson, et al. 2013, *The Astrophysical Journal*, 773, 90.

Horne, K., B. M. Peterson, S. J. Collier, et al. 2004, *Publications of the Astronomical Society of the Pacific*, 116, 465.

Hubble Advanced Spectral Products (HASP) (2025). Space Telescope Science Institute. URL: https://archive.stsci.edu/missions-and-data/hst/hasp (visited on 09/17/2024).

Institute, Space Telescope Science (2025). *STIS Instrument Handbook: Gratings.* URL: https://hst-docs.stsci.edu/stisihb/chapter-13-spectroscopic-reference-material/13-3-gratings (visited on 05/12/2025).

Keel, Bill (2002). *Quasars and Active Galactic Nuclei - Optical spectra of various kinds of active galactic nuclei.* Accessed: 2025-12-22. URL: https://pages.astronomy.ua.edu/keel/agn/spectra.html.

Kollatschny, W. & M. Dietrich 1997, *Astronomy and Astrophysics*, 323, 5–13.

Koss, M. J., C. Ricci, B. Trakhtenbrot, et al. 2022, *The Astrophysical Journal Supplement Series*, 261, 2.

McHardy, I. M., S. D. Connolly, B. M. Peterson, et al. 2017, *Monthly Notices of the Royal Astronomical Society*, 465, 273–289.

McHardy, IM, SD Connolly, K Horne, et al. 2018, *Monthly Notices of the Royal Astronomical Society*, 480, 2881–2897.

Mikulski Archive for Space Telescopes (MAST) (2025). Space Telescope Science Institute. URL: https://mast.stsci.edu/search/ui/#/hst (visited on 09/17/2024).

Mo, H., F. van den Bosch, & S. White 2010, *Galaxy Formation and Evolution*, Cambridge University Press.

Netzer, H. 2013, *The Physics and Evolution of Active Galactic Nuclei*, Cambridge University Press, Cambridge.

Netzer, H. & M. V. Penston 1976, *Monthly Notices of the Royal Astronomical Society*, 174, 319–325.

Ochmann, M. W., W. Kollatschny, M. A. Probst, et al. 2024, *Astronomy & Astrophysics*, 686, A17.

Ochmann, M. W., P. M. Weilbacher, M. A. Probst, et al. 2025, *Astronomy & Astrophysics*, 697, L5.

Onken, C. A., L. Ferrarese, D. Merritt, et al. 2004, *The Astrophysical Journal*, 615, 645–651.

Osterbrock, D. E. 1977, *The Astrophysical Journal*, 215, 733–745.

Osterbrock, D. E. 1981, *The Astrophysical Journal*, 249, 462–470.

Osterbrock, Donald E. & Richard W. Pogge 1985, *The Astrophysical Journal*, 297, 166–176.

Peterson, B. M. 1993, *Publications of the Astronomical Society of the Pacific*, 105, 247–268.

Peterson, B. M. 1997, *An Introduction to Active Galactic Nuclei*, Cambridge University Press.

Peterson, B. M., L. Ferrarese, K. M. Gilbert, et al. 2004, *The Astrophysical Journal*, 613, 682–699.

Peterson, B. M. & K. Horne 2004, *Astronomische Nachrichten*, 325, 248–251.

Peterson, B. M., I. Wanders, K. Horne, et al. 1998, *Publications of the Astronomical Society of the Pacific*, 110, 660.

Peterson, Bradley M. 2011, *Masses of Black Holes in Active Galactic Nuclei: Implications for NLS1s*, URL: https://arxiv.org/abs/1109.4181.

Probst, M. A., W. Kollatschny, M. W. Ochmann, et al. 2025, *Emission-Line and Continuum Reverberation Mapping of the NLS1 Galaxy WPVS 48*, URL: https://arxiv.org/abs/2511.09153.

Rees, M. J. 1984, *Annual Review of Astronomy and Astrophysics*, 22, 471–506.

Ricci, C. & B. Trakhtenbrot 2023, *Nature Astronomy*, 7, 1282–1294.

Rodriguez-Pascual, PM, D Alloin, J Clavel, et al. 1997, *The Astrophysical Journal Supplement Series*, 110, 9.

Seyfert, Carl K. 1943, *The Astrophysical Journal*, 97, 28–40.

Shakura, N. I. & R. A. Sunyaev 1973, *Astronomy and Astrophysics*, 24, 337–355.

STScI (2025). *Digitized Sky Survey*. IPAC. DOI: 10.26131/IRSA441. URL: https://www.ipac.caltech.edu/doi/irsa/10.26131/IRSA441 (visited on 07/19/2025).

Ulrich, M.-H., L. Maraschi, & C. M. Urry 1997, *Annual Review of Astronomy and Astrophysics*, 35, 445–502.

Urry, C. M. & P. Padovani 1995, *Publications of the Astronomical Society of the Pacific*, 107, 803–845.